



Promoting Intratumoral Drug Accumulation by Bio-Membrane Regulated Active Targeting for Tumor Photothermal Therapy

Chenkai Yang ^{1,*}, Xiangqian Cao ^{1,*}, Lei He^{2,3,*}, Cong Wu^{2,*}, Mengxin Zhao², Fei Duan², Zhiwen Qiu², Xiaodong Zhu², Yilin Yan¹, Shengzhou Li¹, Wei Li², Bing Shen ¹

¹Department of Urology, Shanghai General Hospital, Shanghai Jiaotong University School of Medicine, Shanghai, People's Republic of China;

²Department of Nanomedicine & Shanghai Key Laboratory of Cell Engineering, Naval Medical University, Shanghai, People's Republic of China; ³School of Health Science and Engineering, University of Shanghai for Science and Technology, Shanghai, People's Republic of China

*These authors contributed equally to this work

Correspondence: Wei Li, Department of Nanomedicine & Shanghai Key Laboratory of Cell Engineering, Naval Medical University, 800 Xiangyin Road, Yangpu District, Shanghai, 200433, People's Republic of China, Tel +86 21 81871644, Fax +86 21 81870801, Email liwei_dds@163.com; Bing Shen, Department of Urology, Shanghai General Hospital, Shanghai Jiaotong University School of Medicine, 85 Wujin Road, Hongkou District, Shanghai, 200080, People's Republic of China, Tel/Fax +86 18017181979, Email urodrshenbing@shsmu.edu.cn

Introduction: Insufficient tumor permeability and inadequate nanoparticle retention continue to be significant limitations in the efficacy of anti-tumor drug therapy. Numerous studies have focused on enhancing tumor perfusion by improvement of tumor-induced endothelial leakage, often known as the enhanced permeability and retention (EPR) effect. However, these approaches have produced suboptimal therapeutic outcomes and have been associated with significant side effects. Therefore, in this study, we prepared tumor cell membrane-coated gold nanorods (GNR@TM) to enhance drug delivery in tumors through homogeneous targeting of tumor cell membranes and in situ real-time photo-controlled therapy.

Methods: Here, we fabricated GNR@TM, and characterized it using various techniques including Ultraviolet-Visible (UV-Vis) spectrophotometer, particle size analysis, potential measurement, and transmission electron microscopy (TEM). The cellular uptake and cytotoxicity of GNR@TM were analyzed by flow cytometry, confocal laser scanning microscopy (CLSM), TEM, CCK8 assay and live/dead staining. Tissue drug distribution was determined by inductively coupled plasma mass spectrometry (ICP-MS) and immunofluorescence staining. Furthermore, to evaluate the therapeutic effect, mice bearing MB49 tumors were intravenously administered with GNR@TM. Subsequently, near-infrared (NIR) laser therapy was performed, and the mice's tumor growth and body weight were monitored.

Results: The tumor cell membrane coating endowed GNR@TM with extended circulation time in vivo and homotypic targeting to tumor, thereby enhancing the accumulation of GNR@TM within tumors. Upon 780 nm laser, GNR@TM exhibited excellent photothermal conversion capability, leading to increased tumor vascular leakage. This magnification of the EPR effect induced by NIR laser further increased the accumulation of GNR@TM at the tumor site, demonstrating strong antitumor effects in vivo.

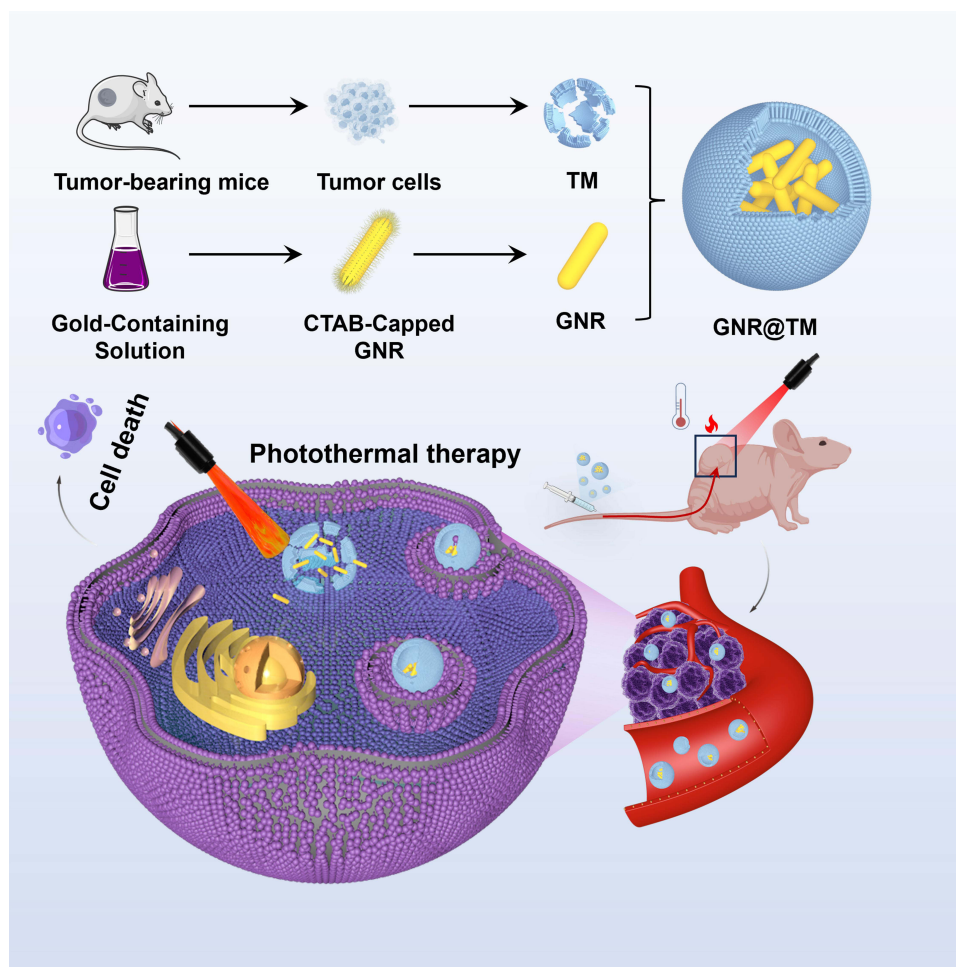
Conclusion: In this study, we successfully developed a NIR-triggered nanomedicine that increased drug accumulation in tumor through photo-controlled therapy and homotypic targeting of the tumor cell membrane. GNR@TM has been demonstrated effective suppression of tumor growth, excellent biocompatibility, and significant potential for clinical applications.

Keywords: intratumor drug accumulation, photo-controlled therapy, homotypic targeting, tumor cell membrane, gold nanorods

Introduction

Traditional anti-cancer drugs exhibit a number of limitations in clinical practice, including off-target effects on normal tissues and inadequate accumulation at tumor sites.^{1,2} Cancer nanomedicines have been specifically engineered to avoid the pharmacokinetic constraints associated with conventional drugs.³ Nanomedicines can selectively accumulate in tumor tissues through the enhanced permeability and retention (EPR) effect of tumors, which is a result of the abnormal leakage

Graphical Abstract



of blood vessels and inadequate drainage of lymphatic system in tumors.⁴ In comparison to conventional chemotherapeutics, these nanomedicines have been demonstrated to have numerous advantages, such as, enhanced drug solubility, extended circulation *in vivo*, augmented bioavailability, and significantly mitigated adverse effects associated with the parent drugs.⁵ However, as a passive targeting strategy, the EPR effect is limited for drug delivery, and in most cases, achieving sufficient accumulation of nanomedicines is not feasible in solid tumors, resulting in low therapeutic efficacy.^{6,7} In addition, in poor permeability tumors, active trans-endothelial transport is the main pathway for nanomedicines to enter the tumor.^{8,9}

There are several obstacles in the transport process of nanomedicines to tumor cells, such as fast elimination from the bloodstream and non-specific absorption by normal cells.¹⁰ A multitude of tumor-targeting ligands, including antibodies, single-chain fragments of antibodies, sugar molecules, and simplified peptide sequences,^{11–13} have been introduced into nano-systems for active targeting through receptor-mediated endocytosis (RME),¹⁴ which exhibits improved treatment effectiveness and reduced toxicity. Recently, the utilization of cell membranes for surface modification of nanoparticles has gained prominence as a novel strategy for drug delivery, immune modulation, and vaccine administration.^{15,16} For instance, the surface modification of nanoparticles with platelet membranes bestows augmented tumor targeting capability to nanomedicines, enabling accurate tumor ablation.¹⁷ Similarly, hybrid cell membranes of platelet membranes and pH-responsive vesicles enable nanomedicines to maintain stability in the bloodstream and accumulate at the tumor

site through active and passive targeting capabilities.¹⁸ Tumor cells exhibit distinctive characteristics, including antigen presentation and homotypic targeting, which are influenced by transmembrane proteins on their surface, such as pan-cadherin, carcinoembryonic antigen, or galectin-3.¹⁹ The cancer cell membrane can endow nanoparticles with immune evasion and homotypic targeting abilities for precise and potent cancer therapy.^{19–22}

Photothermal therapy (PTT) based on NIR laser is a novel cancer treatment method that offers unique advantages of minimally invasive and precise treatment.²³ PTT utilizes a photosensitizer to generate heat, which is used for thermal ablation of cancer cells under NIR laser irradiation. Thanks to nanotechnology, the surface functionalization and the ability to carry multiple drugs of nanomaterials enable the integration of diverse functions into one system.²⁴ Gold nanorods (GNRs) are widely used in biological imaging, disease diagnosis, and cancer treatment due to their biological-related features, high biocompatibility, and stability.²⁵ Especially based on the local surface plasmon resonance (LSPR) effect, it has excellent photothermal conversion ability and has become an excellent candidate material in PTT.²⁶ For instance, a cancer cell membrane-derived nanocarrier (mCas9-sGNRs) has been employed for synergistic photothermal/gene therapy (PTT/GT), with gold nanorods (GNRs) serving as the PTT agent and the carrier for sgRNA.²⁷

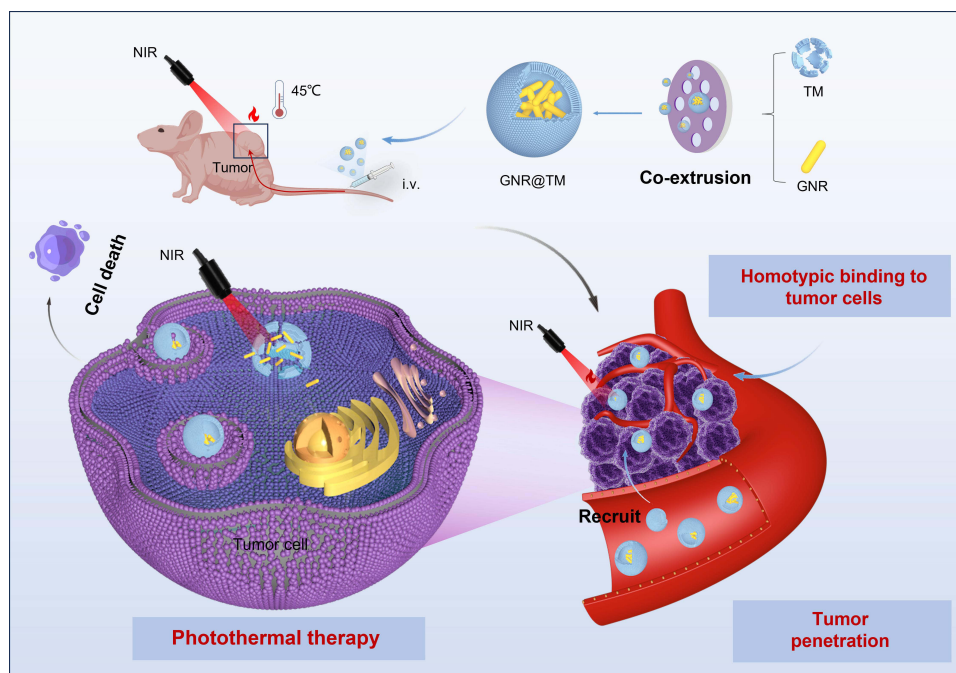
The penetration of nanomedicines within tumors is a critical step in drug delivery, exerting a significant impact on anti-tumor therapy. Firstly, throughout intravascular transport, obstacles to blood perfusion primarily stem from irregular vasculature and accumulated solid stress. Secondly, during transvascular transport, the primary transport impediments include increased interstitial fluid pressure (IFP) and limited interendothelial gaps. Thirdly, the dense extracellular matrix (ECM), abnormal blood vessels, and binding site barriers impede the extravascular transport of nanoparticles.²⁸ Many strategies have shown that vasodilation induced by nitric oxide donors,²⁹ disruption of the vascular barrier mediated by specific depletion of tumor-associated platelets,³⁰ tumor hemorrhagic strategies involving vascular disruptors,³¹ and loss of endothelial adhesion junctions activated by gold nanoparticles inducing endothelial leakage (NanoEL)³² are used to magnify the EPR effect for improvement of tumor permeability and the delivery efficiency of anti-tumor drugs.^{33,34} However, for these strategies, there is a potential risk of inducing endothelial leakage in normal tissue blood vessels to cause drug accumulation in non-targeted sites, leading to adverse reactions, and uncertain clinical outcomes.³⁵ Recent studies have shown that hyperthermia can increase tumor blood flow and extravasation,³⁶ which could further facilitate drug accumulation in tumor. Therefore, the utilization of laser-induced local irradiation of the tumor site to induce tumor vascular endothelial leakage is an ideal choice because of enhanced accumulation of drugs at tumor site rather than normal tissue.

In this study, GNRs were synthesized and functionalized with tumor cell membrane (TM) to obtain GNR@TM with excellent biocompatibility and targeting ability (Scheme 1). The tumor cell membrane enhanced prolonged circulation time of GNRs and their specific recognition capability towards tumors *in vivo*, thereby enhancing the accumulation of GNR@TM within tumors. Furthermore, upon 780 nm laser, GNR@TM could induce endothelial leakage in primary tumor blood vessels, leading to an increased drug leakage from the tumor vascular system into the interstitial space, without affecting healthy vasculature. The magnification of the EPR effect induced by NIR laser further promoted the accumulation of GNR@TM in tumors for effective thermal ablation of the tumor *in vivo*.

Materials and Methods

Materials

Hydrogen tetrachloroaurate (III) (HAuCl₄), L-ascorbic acid, silver nitrate (AgNO₃), cetyltrimethylammonium bromide (CTAB), sodium borohydride (NaBH₄) and fluorescein isothiocyanate (FITC) were purchased from Sigma Aldrich. Roswell Park Memorial Institute (RPMI) 1640 culture medium, Dulbecco modified Eagle medium (DMEM), penicillin-streptomycin, and fetal bovine serum (FBS) were purchased from Gibco. CCK-8 kit was purchased from MCE. BCA protein assay kit, 1,1-dioctadecyl-3,3,3,3-tetramethylindocarbocyanine perchlorate (DIL), apoptosis detection kit, live and dead dye kit were obtained from Beyotime Institute of Biotechnology.



Scheme 1 A schematic representation demonstrating the advantages and application of targeted delivery of GNR@TM in cancer photothermal therapy.

Preparation of TM

To obtain tumor cell membranes, female BALB/c nude mice were inoculated with MB49 bladder tumor cells subcutaneously. After three weeks, when the tumor size reached approximately 500 mm³, the tumor was resected and digested using RPMI 1640 medium containing collagenase IV (1 mg/mL) and DNase I (0.2 mg/mL) at 37 °C. The resulting mixture underwent filtration using a 70-micron filter and centrifuged to collect purified tumor cells. Tumor cells were subjected to hypotonic treatment using a solution comprising 20 mM Tris-HCl (pH 7.5), 10 mM KCl, 2 mM MgCl₂ and 100 μM PMSF for a duration of 2 h at 4 °C. The supernatant was collected by centrifuging at a speed of 3000 g for five minutes at the same temperature. The resulting cell membranes were washed with a solution comprising 10 mM Tris-HCl (pH 7.5) and 1 mM EDTA, followed by resuspension in deionized water and then storage at –80 °C for further experiments. The protein content of the membrane extract was determined by a BCA protein assay kit.

Preparation of GNRs

GNRs were prepared via a seed-mediated growth method using CTAB as previously described.³⁷ In brief, 5 mL of warm 0.2 M CTAB was mixed with 5 mL of 1 mM HAuCl₄ for the preparation of seed solution. Subsequently, 0.6 mL of ice-cold 10 mM NaBH₄ was introduced into the stirred mixture and vigorously stirred for two minutes before being left unstirred for one hour to acquire a light tan solution. For the growth solution, 5 mL of 0.2 M CTAB, 5 mL of 1 mM HAuCl₄, 250 μL of 4 mM AgNO₃, and 75 μL of 80 mM ascorbic acid were successively added to a beaker under gentle stirring in sequence. After the color of the solution faded, 20 μL of the seed solution was gently introduced into the growth solution and stirred. The mixture was left at room temperature for 12 hours, then purified through two rounds of centrifugation (to eliminate excess CTAB) at 12,000 g for 20 minutes before being resuspended in deionized water.

Preparation and Characterization of GNR@TM

To prepare GNR@TM, 400 μg of TM (protein weight) was mixed with GNR (5 mg/mL) and stirred for 1 h. The solution was then sonicated for 25 minutes (110 W, 25 °C) and physically extruded 11 times using an Avanti mini extruder with a 450 nm polycarbonate membrane. The unencapsulated GNRs were removed by passing through a 450 nm filter (negatively charged). The mixture was then centrifuged (12,000 g, 10 min, 4 °C) and subjected to overnight dialysis to collect GNR@TM.

The Zetasizer Nano ZS dynamic light scattering instrument (DLS, Malvern, UK) was utilized to measure ζ potential, hydrodynamic size distribution, and polydispersity index (PDI). The light absorption curve was measured using the Cary 300 Ultraviolet-Visible (UV-Vis) spectrophotometer. Transmission electron microscopy (TEM) was employed to observe the morphology of GNR@TM.

Preparation and Characterization of GNR@Lipo

Firstly, 5 mg of 1,2-dioleoyl-sn-glycero-3-phosphocholine (DOPC) was weighed and dissolved in 1 mL absolute ethanol. Next, the DOPC was transferred to a rotary evaporator and spin-coated at 80 r/min at 37 °C to form a film. Then, a suspension was formed by adding 2 mL of the prepared GNR aqueous solution (2.5 mg/mL) to the rotary evaporator mentioned above. The above suspension was sonicated for 25 min (110 W, 25 °C) and then physically extruded 11 times with an Avanti mini extruder through a 450 nm polycarbonate membrane. Unencapsulated GNR was removed through a 400 filter (negative charge). Finally, the obtained GNR@Lipo (GNR@Liposome) was characterized.

Stability Analysis of GNR@TM and GNR@Lipo

GNR@Lipo (1 mg/mL) and GNR@TM (1 mg/mL) were suspended in PBS and RPMI 1640 cell culture medium supplemented with 10% FBS for 21 days, and DLS was used to measure the hydrodynamic sizes of GNR@Lipo and GNR@TM at various time points.

In vitro Photothermal Efficiency

GNR, GNR@Lipo, and GNR@TM were distributed in a PBS solution at an equivalent concentration (50 $\mu\text{g/mL}$ for GNR). Next, the samples were exposed to a 780 nm laser with an intensity of 1.5 W/cm^2 for 5 minutes. Real-time thermographic images and temperature changes were captured by an infrared camera. The analysis of consecutive irradiation-cooling was conducted by exposing the samples to radiation for 5 minutes, followed by cooling to room temperature. The values were then measured by an infrared camera.

Cell Culture

Murine bladder cancer cell (MB49) and 293T cells were acquired from American Type Culture Collection. MB49 cells were cultivated in RPMI 1640 medium supplemented with 10% FBS and 1% penicillin-streptomycin under 5% CO_2 at 37 °C. 293T cells were cultured in DMEM supplemented with 10% FBS and 1% penicillin-streptomycin in the presence of 5% CO_2 at 37 °C.

Cell Uptake of GNR@TM

MB49 cells were plated in 6-well plates (5×10^5 cells per well) and incubated for 12 h. FITC labeled GNR (20 $\mu\text{g/mL}$), GNR@Lipo (20 $\mu\text{g/mL}$) and GNR@TM (20 $\mu\text{g/mL}$) were added to co-culture with MB49 cells for 4 h. The mean fluorescence intensity was measured by flow cytometry.

In addition, MB49 cells were seeded in confocal dishes (5×10^5 cells per dish). FITC (1 $\mu\text{g}/\mu\text{L}$, 100 μL) was co-incubated with GNR for 1 hour, followed by three washes with ultrapure water to obtain FITC-labeled GNR. DIL was used to mark TM, then fluorescein-labeled GNR (20 $\mu\text{g/mL}$), GNR@Lipo (20 $\mu\text{g/mL}$) and GNR@TM (20 $\mu\text{g/mL}$) were added and co-cultured for 4 h. The cell nuclei were stained with Hoechst 33342 and the distribution of fluorescence signals was observed by confocal laser scanning microscopy (CLSM).

The distribution of GNR in cells was observed by TEM. After culture with GNR for 12 h, cells were fixed with 2.5% glutaraldehyde. After washing with phosphate buffer, the cells were fixed with 1% osmium acid at room temperature for 2 h. The samples were dehydrated in a graded series of ethanol, embedded in epoxy resin, cut into ultrathin sections, stained with uranyl acetate and lead citrate, and finally imaged on TEM.

Cytotoxicity Assay

Cell viability was assessed by Cell Counting Kit-8 (CCK8, MCE, USA). MB49 and 293T cells were seeded into 96-well plates (5000 cells per well) with 100 μL medium. Then, PBS, GNR (0–108 $\mu\text{g/mL}$), GNR@Lipo (0–108 $\mu\text{g/mL}$) and

GNR@TM (0–108 $\mu\text{g}/\text{mL}$) were co-cultured with MB49 cells and 293T cells for 24h, and exposed to 780 nm laser (1.5 W/cm^2 , 5 min) or not. Then, 10 μL CCK-8 reagent was added to each well and incubated for 2 h. Cell viability was assessed by quantifying the absorbance at 450 nm with a microplate reader.

Live-Dead Staining

MB49 cells were seeded into confocal dishes (5×10^5 cells per dish). Then, PBS, GNR (50 $\mu\text{g}/\text{mL}$), GNR@Lipo (50 $\mu\text{g}/\text{mL}$) and GNR@TM (50 $\mu\text{g}/\text{mL}$) were co-cultured with MB49 cell for 24 h. After that, cells were irradiated with/without 780 nm laser (1.5 W/cm^2 , 5 min). Then, all cells were stained with Calcein AM and PI for 30 min under 37 °C, followed by being observed by a confocal microscope.

Cell Apoptosis Analysis

MB49 cells were grown adherent to the wall in 6-well plates at a density of 5×10^5 cells per well and treated with PBS, GNR (50 $\mu\text{g}/\text{mL}$), GNR@Lipo (50 $\mu\text{g}/\text{mL}$) and GNR@TM (50 $\mu\text{g}/\text{mL}$) for 24 h. Then, cells were irradiated with 780 nm laser or not (1.5 W/cm^2 , 5 min). After further incubation for six hours, cells were harvested, stained with Annexin V-FITC (5 μL) and PI (10 μL), and finally analyzed by flow cytometry. For flow cytometry analysis, a gating strategy was employed to selectively include viable cells, and 10,000 cells per experimental group were collected for subsequent analysis. Late apoptosis (Annexin-V+/PI+ cells) rates were analyzed using FlowJo software.

Animals Model

All animal experiments were conducted in accordance with the Regulations for the Administration of Affairs Concerning Experimental Animals, which were approved by the State Council of the People's Republic of China. All animal procedures were reviewed and ethically approved by Shanghai General Hospital Medical Ethics Committee (2020SQ159-3).

The in vivo antitumor assay was evaluated using murine models bearing MB49 tumors, and BALB/c mice were subcutaneously injected with 1×10^6 MB49 cells into the right flank.

Hemolysis Assay

Blood samples were obtained from normal BALB/c nude mice and centrifuged for 5 minutes (3500 rpm). Then, the pellet was washed 5 times, and purified RBCs were diluted in PBS. Next, 200 μL of erythrocytes suspension was added to PBS, GNR (50 $\mu\text{g}/\text{mL}$), GNR@Lipo (50 $\mu\text{g}/\text{mL}$) and GNR@TM (50 $\mu\text{g}/\text{mL}$) severally (0.5 h, 37 °C, 500 rpm). Afterwards, the solution was centrifuged (3500 rpm, 5 minutes) and 100 μL of supernatant was added to a 96-well plate to quantify the absorbance at 540 nm. The percent hemolysis was calculated using the following formula: Hemolysis (%) = (sample absorbance-negative control absorbance)/(positive control absorbance-negative control absorbance) $\times 100$.

Blood Pharmacokinetic Studies

BALB/c nude mice ($n = 3$) were subcutaneously inoculated with MB49 cells. On day 10 after tumor inoculation, when the tumor volume was approximately 150 mm^3 , GNR (50 $\mu\text{g}/\text{mL}$) and GNR@TM (50 $\mu\text{g}/\text{mL}$) were administered intravenously at a dose of 2 mg/kg, respectively, with or without 780 nm laser treated (1.5 W/cm^2 , 5 min). At predetermined time points (1 min, 0.5 h, 12 h, 24 h, and 48 h), blood samples (100 μL) were collected from the orbital vein. The gold concentration in the collected blood was measured using ICP-MS. Standards were prepared and measured with samples to quantify gold concentrations in blood as percent injected dose per gram of tissue (%ID/g).

Tissue Biodistribution

Nude mice bearing MB49 were injected with GNR, GNR@Lipo, GNR@TM through the tail vein, and the tumor was irradiated with or without 780 nm laser (1.5 W/cm^2 , 5 min). After 24 h, mice were euthanized and major organs (heart, liver, spleen, lung and kidney) as well as tumors were obtained to measure gold content ex vivo by ICP-MS.

In vivo Photothermal Efficiency

Nude mice bearing MB49 tumors were treated with PBS, GNR, GNR@Lipo, GNR@TM, and the tumors were exposed to 780 nm laser (1.5 W/cm^2) for 5 min. Throughout the procedure, we monitored the temperature changes and took images with an infrared camera.

In vivo Antitumor Efficacy

To establish the MB49 tumor model, MB49 cells (1×10^6) were subcutaneously injected into the right flank of each mouse. When the size reached 150 mm^3 (after 10 days), mice were divided into eight groups in a random manner and subjected to different interventions (every two days for 5 times: PBS, GNR, GNR@Lipo, GNR@TM, PBS/L, GNR/L, GNR@Lipo/L, GNR@TM/L (L represented the laser irradiation, 780 nm, 1.5 W/cm^2 , 5 min)). The body weight was measured every other day, and the tumor volume (V) was determined by “length \times width² /2”. When the tumor volume exceeded 1200 mm^3 , mice were sacrificed, and major organs and tumors were acquired for further histopathological and immunofluorescent analysis.

Statistical Analysis

Statistical analyses were performed with GraphPad Prism. Three independent experiments were conducted at a minimum. Experimental data is expressed as mean \pm SD. Statistical significance was calculated via one-way or two-way ANOVA: $P < 0.05$ level was considered statistically significant.

Results

Synthesis, Characterization and in vitro Photothermal Efficiency of GNR@TM

Here, GNRs were prepared via a seed-mediated growth method, and TM was extracted through hypotonic lysis. Subsequently, GNR@TM hybrids were successfully prepared by ultrasonication and coextrusion with a 400 nm filter (Figure 1A). The UV–Vis spectrophotometer scan revealed a distinctive absorption peak at 780 nm for GNR (Figure 1B). Then, the photothermal conversion performance of GNR@TM was evaluated under laser irradiation at 780 nm. When exposed to 780 nm laser (1.5 W/cm^2 , 5 min), solutions containing PBS, GNR, GNR@Lipo and GNR@TM exhibited a rapid temperature increase to approximately $55 \text{ }^\circ\text{C}$, indicating high photothermal conversion efficiency (Figures 1C and S1). Notably, GNR@TM achieved a higher temperature than that of GNR@Lipo (approximately $51 \text{ }^\circ\text{C}$), but slightly lower than that of GNR (approximately $57 \text{ }^\circ\text{C}$). To investigate the thermal stability under light irradiation, consecutive irradiation-cooling experiments were performed (Figure 1D). The solutions were subjected to a 780 nm laser (5 min) and then cooled to room temperature. The GNR@TM solution maintained its stable temperature throughout three rounds of laser, showcasing the exceptional photothermal stability of GNR@TM. The similar photothermal heating curve (Figure 1B) and the slight shift of the absorption peak towards shorter wavelengths (Figure 1C) for GNR@Lipo or GNR@TM indicated successful encapsulation of GNR.

Moreover, dispersion studies were conducted for 21 days in PBS solution and RPMI 1640 medium with 10% FBS, demonstrated excellent stability of both GNR@Lipo and GNR@TM formulations, as evidenced by consistent hydrodynamic sizes and low PDI values monitored using DLS technique at various time points (Figures 1E and S2). TEM revealed that GNR presented as a dark, short rod-shaped structure with blunt, rounded ends, while GNR@TM was encased by a thin membrane layer (Figure 1H). Besides, both DLS analysis and ζ potential confirmed the successful preparation of GNR@TM, as evidenced by the increase in particle size (Figure 1F) and the decrease in surface charge to the level of TM (Figure 1G) after encapsulation. After laser irradiation, the size of GNR@TM increased, indicating that the fragmented cell membrane dispersed the particle size of the material, which was beneficial for the exposure of GNR and may contribute to enhanced uptake by tumor cells and improved photothermal performance.

Cell Uptake

The cell uptake of GNR@TM was initially assessed via flow cytometry. In Figure 2A and B, the absorption rate of GNR@TM was markedly higher than that of GNR@Lipo and GNR. The TM coating on the surface of GNR@TM was

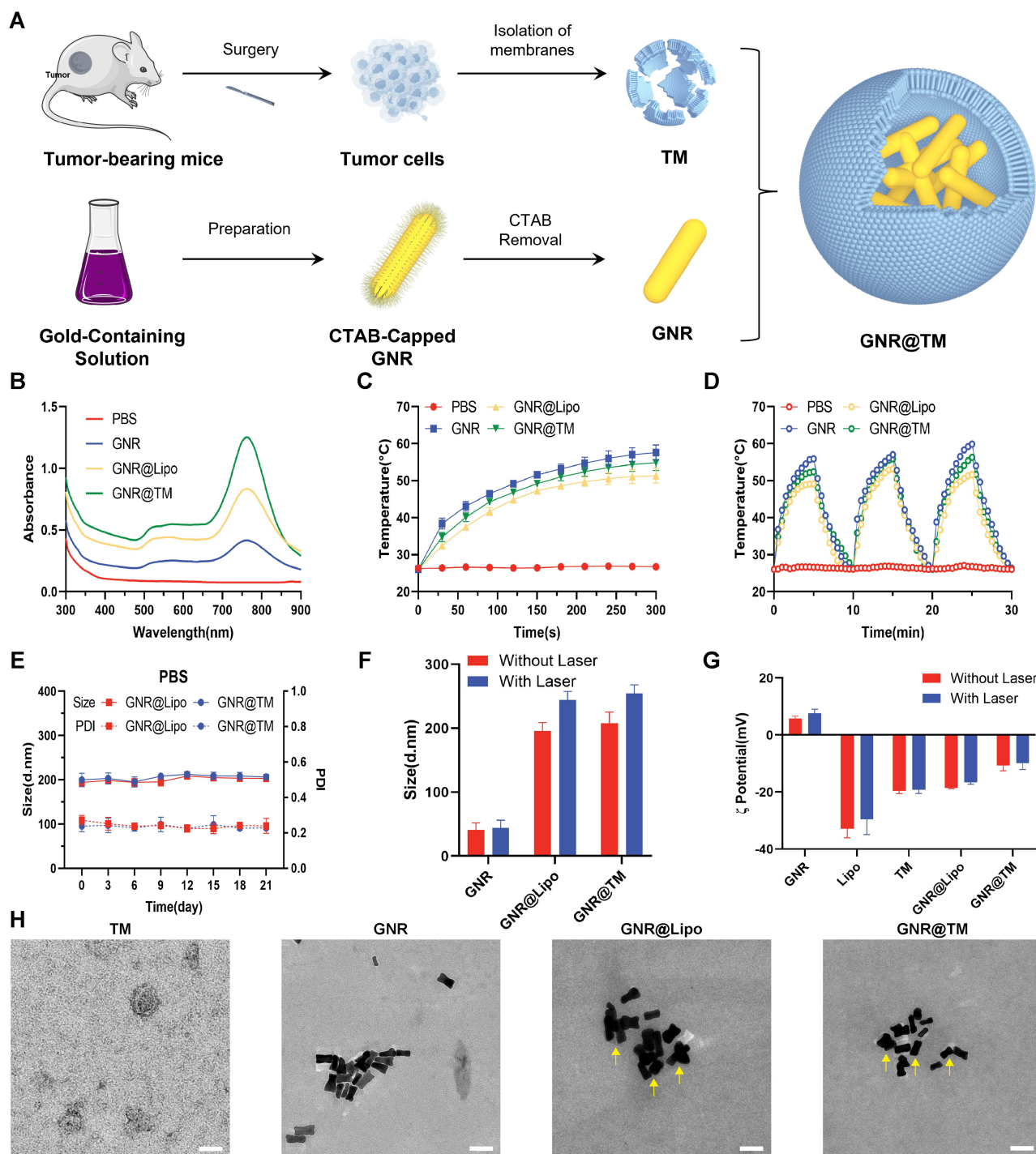


Figure 1 Preparation and characterization of GNR@TM. (A) A schematic diagram illustrating the synthesis and the structure of GNR@TM. (B) UV absorption spectrum of PBS, GNR, GNR@Lipo and GNR@TM. (C) Temperature changes of PBS, GNR, GNR@Lipo and GNR@TM under 780nm laser (1.5 W/cm², 5 min) (n = 3). (D) Temperature changes of PBS, GNR, GNR@Lipo and GNR@TM during three on/off cycles of laser irradiation. (E) The size and PDI changes of GNR@Lipo and GNR@TM in PBS for 3 weeks (n = 3). (F) Size and ζ potential of GNR, GNR@Lipo and GNR@TM with or without NIR laser irradiation (1.5 W/cm², 5 min) (n = 3). (G) ζ potential of GNR, Lipo, TM, GNR@Lipo and GNR@TM with or without NIR laser irradiation (1.5 W/cm², 5 min) (n = 3). (H) Representative TEM images of TM, GNR, GNR@Lipo and GNR@TM (arrow headed). Scale bar: 50 nm.

obtained from MB49 cells, possessing a targeted affinity towards MB49 cells.^{38,39} Colocalization analysis with CLSM was also conducted (Figures 2C and S3), where FITC-labeled GNR and DIL-labeled TM were utilized to form GNR@TM that underwent co-incubation with MB49 cells. The presence of both fluorescences further confirmed successful cellular entry of GNR@TM.

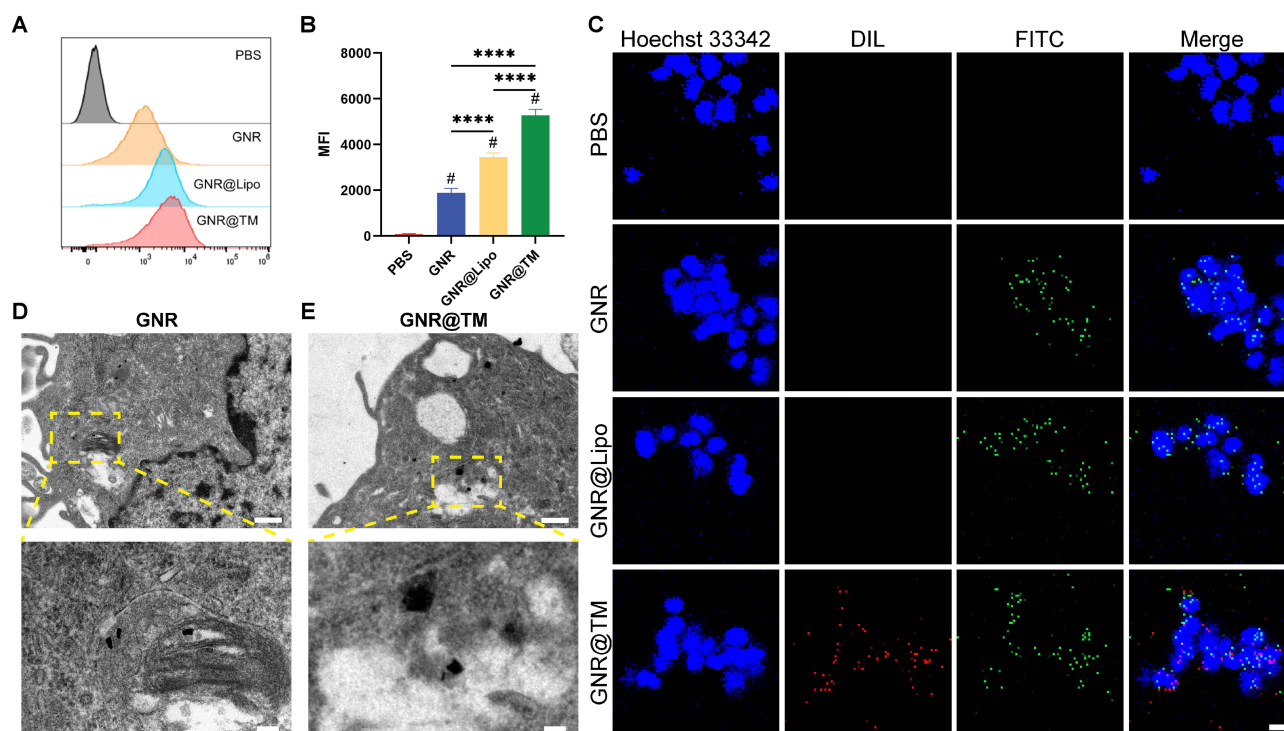


Figure 2 In vitro cell uptake of GNR@TM. (A) Flow cytometric analysis of MB49 cells after treatment with PBS, GNR, GNR@Lipo and GNR@TM respectively and (B) corresponding mean fluorescence intensity (MFI) ($n = 3$). (C) The CLSM images of MB49 cells after treatment with PBS, GNR, GNR@Lipo and GNR@TM, respectively. GNR, GNR in GNR@Lipo and GNR in GNR@TM were stained with FITC, TM in GNR@TM was stained with DIL and the cell nuclei were stained with Hoechst 33,342. Scale bar: 10 μm . Representative TEM images of MB49 cells treated with GNR (D) and GNR@TM (E) for 24 h (The scale bar is 500 nm in the upper images and 100 nm in the lower enlarged images). # $P < 0.0001$ (# vs PBS group). **** $P < 0.0001$.

To further investigate the endocytosis of GNR@TM by MB49 cells, cellular internalization was observed via TEM. As shown in Figure 2D, GNRs located proximal to the plasma membrane were phagocytosed by MB49 tumor cells, which were subsequently sequestered within intracellular lysosomes before escaping into the cytoplasm and ultimately being transported to mitochondria.^{40,41} Simultaneously, GNR@TM was transported into the cells in clustered form from the vicinity of the plasma membrane, which may be attributed to the targeting ability induced by the camouflage membrane (Figure 2E). These findings were consistent with the results obtained from CLSM. Furthermore, all organelles were found to be in optimal condition and easily distinguishable, as observed in control cells (Figure S4). These results suggested that the tumor cell membrane may efficiently facilitate the uptake of GNR without causing significant cellular damage.

Cytotoxicity Analysis

The biocompatibility of GNR, GNR@Lipo and GNR@TM was confirmed through CCK8 assay on two cell lines (MB49 tumor cells and 293T kidney epithelial cells) (Figure 3A–F). Following a 24-hour incubation period without laser exposure, both cell viability exceeded 80% at a concentration of 108 $\mu\text{g/mL}$. However, significant cytotoxicity was observed under laser irradiation due to the PTT effect, resulting in approximately 50% of tumor cell death at a concentration of 54 $\mu\text{g/mL}$ GNR@TM. At the same concentration, GNR@TM exhibited stronger phototoxicity than GNR and GNR@Lipo, which may be due to stronger cellular internalization or photothermal properties. Interestingly, more MB49 cells died upon the same PTT conditions compared with 293T cells, indicating a heightened susceptibility of tumor cells to thermal stimulation, as previously reported.⁴²

Utterly, the impact of GNR@TM-mediated PTT on tumor cells was evaluated by live/dead cell staining (Figures 3G and S5). MB49 cells were subjected to double-staining with Calcein AM and PI for direct visualization of live and dead cells, respectively. No cytotoxicity was detected in the PBS, GNR, GNR@Lipo or PBS/L groups as evidenced by green fluorescence indicating live cells. In contrast, most cells were killed and showed a large amount of red fluorescence (dead cells) in the GNR@TM/L group. Due to inadequate cellular internalization or suboptimal

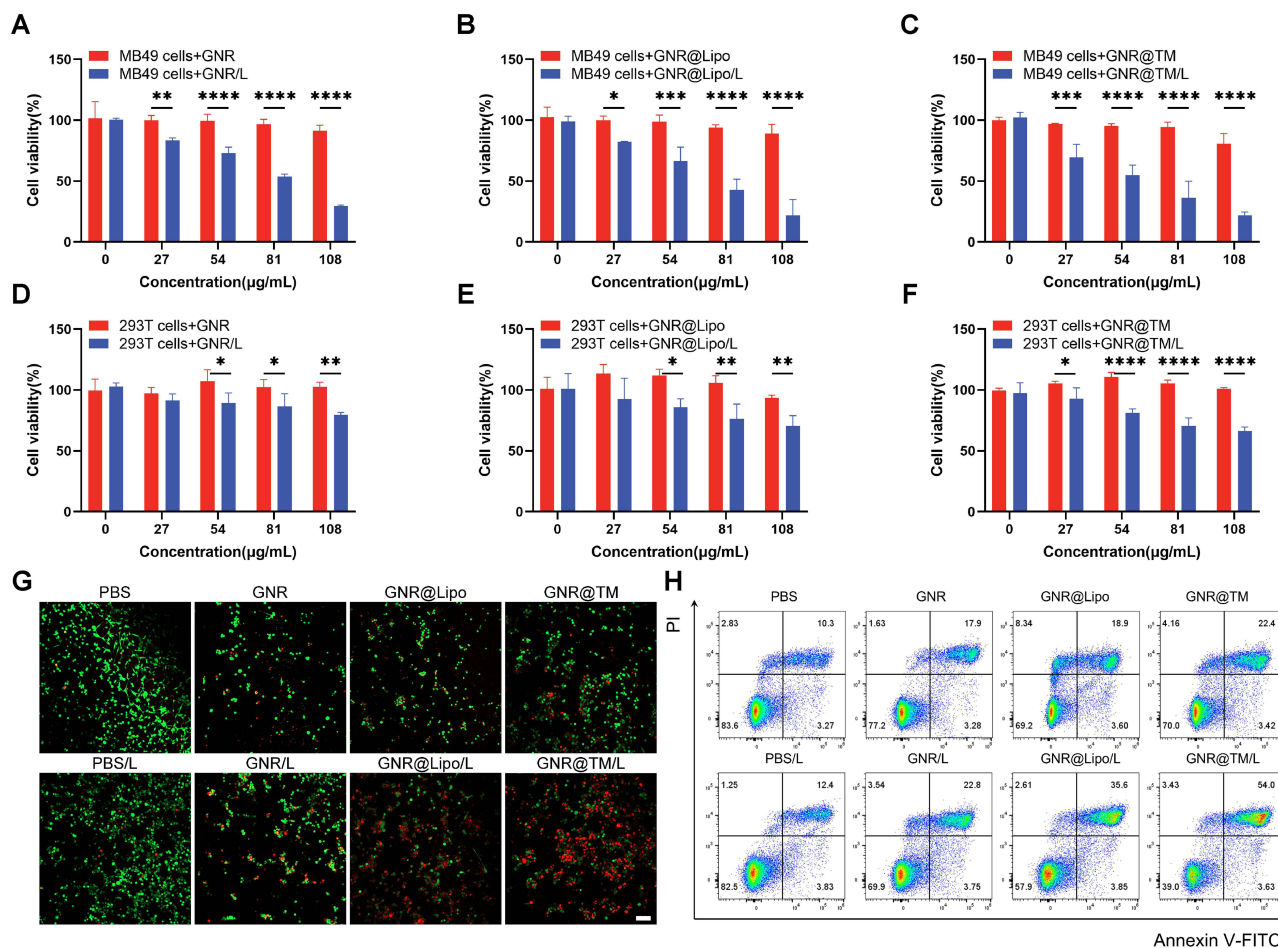


Figure 3 In vitro antitumor effect of GNR@TM. (A–C) Cell viability of MB49 cells after GNR, GNR@Lipo or GNR@TM co-culturation with/without laser (n = 3). (D–F) Cell viability of 293T cells after GNR, GNR@Lipo or GNR@TM co-incubation under laser irradiation or not (n = 3). (G) The CLSM images of Calcein AM (green) and propidium iodide (PI, red) stained MB49 cells after different treatments. Scale bar: 100 µm. (H) Flow cytometry-based apoptotic analysis of MB49 cells after different treatments. *P < 0.05, **P < 0.01, ***P < 0.001, and ****P < 0.0001.

photothermal performance, the efficacy of photothermal killing was significantly compromised in both the GNR/L and GNR@Lipo/L group.

To further investigate the fate of cell death following various treatments, flow cytometry was conducted (Figure 3H). Treatment with GNR/L resulted in a late apoptotic population of 22.8% (Annexin-V-FITC+/PI+). The cell exhibited an increase upon treatment with GNR@Lipo/L, resulting in a late apoptotic rate of 35.6%. Subsequently, the late apoptotic population was further augmented by the administration of GNR@TM/L, ultimately culminating in a late apoptotic rate of 55.3% at the same dosage.

Hence, it can be deduced that GNR@TM exhibits promising potential in PTT for tumors owing to its targeting and photothermal advantages.

Biosecurity, Pharmacokinetics and Biodistribution

Prior to clinical trials, the consideration of biosecurity is necessary. Therefore, red blood cells were collected for hemolysis analysis (Figures 4A, B and S6), which demonstrated that GNR@TM exhibited a negligibly low hemolysis rate with or without laser irradiation, indicating its excellent biocompatibility.

The majority of studies suggest that tumor cell membrane-modified nanomaterials possess the capability to effectively target tumor sites.^{19,43} Based on this premise, we conducted an investigation into the targeting and biodistribution of GNR@TM in mice bearing MB49 tumors. Efficient tumor accumulation requires the prolongation of blood circulation, which was monitored through time-dependent measurement of GNR@TM concentration after intravenous injection

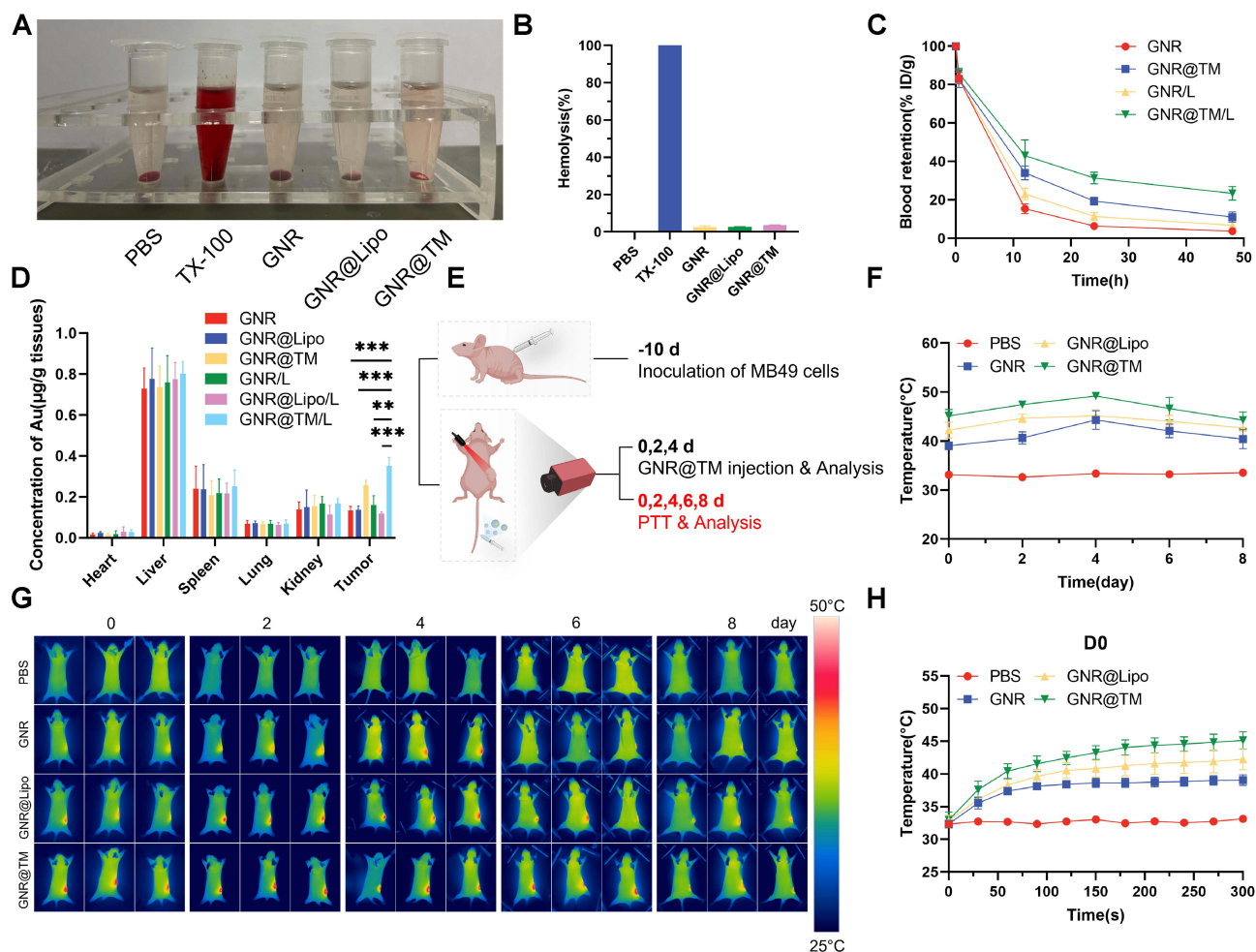


Figure 4 In vivo biodistribution and photothermal efficiency analysis. (A) Pictures and (B) quantification analysis of the hemolysis test after different treatments. TX-100 as a positive control (n = 3). (C) Time-dependent Au element analysis by ICP-MS in plasma within 48 h after GNR or GNR@TM intravenous injection with/without laser irradiation (n = 3). (D) Biodistribution of Au element after intravenous administration with GNR, GNR@Lipo or GNR@TM 24 h later by ICP-MS with/without NIR irradiation (n = 3). (E) Illustration of the timepoints during therapeutic process in MB49-bearing mice with multiple treatments to assess photothermal efficiency in vivo. (F) Peak tumor temperature changes of PBS, GNR, GNR@Lipo and GNR@TM with laser irradiation (1.5 W/cm², 5 min) on different days (n = 3). (G) Infrared thermal images of different groups after laser irradiation (1.5 W/cm², 5 min) on different days (n = 3). (H) Temperature changes at tumor regions during laser irradiation (1.5 W/cm², 5 min) on day 0 (n = 3). **P < 0.01, ***P < 0.001.

(Figure 4C). Within all groups, GNR@TM/L exhibited the longest blood circulation, while the laser group showed a slower clearance rate from the bloodstream compared to the non-laser group. Tissue accumulation of GNR in major organs was determined by ICP-MS after injection for 24 h. The tumors in the GNR@TM/L group exhibited a significantly higher gold concentration (0.35 μg/g) compared to that of the GNR@Lipo/L group (0.12 μg/g) (Figure 4D). These mice exhibited elevated levels of gold in their livers, spleens, and tumors while exhibiting reduced levels of gold in their hearts, lungs and kidneys, as previously reported.^{44,45} The high accumulation of the GNR@TM/L group in tumors can be ascribed to the homotypic binding capacity of cancer membranes enveloping GNR, the extended circulation time of GNR@TM in bloodstream, and the magnification of tumor EPR effect induced by NIR laser.

In vivo Photothermal Efficiency Analysis

To assess the photothermal performance in vivo, an infrared thermal imager was used to monitor the real-time temperature change at tumors following intravenous injection of GNR@TM. A sharp increase in tumor surface temperature was observed across all groups except for the PBS group (Figure 4G and H). Notably, the GNR@TM group exhibited a significantly stronger temperature rise (45 °C) within just five minutes, which can be ascribed to its exceptional tumor targeting and high photothermal conversion efficiency. Subsequently, three administrations and five

irradiations were conducted on alternate days. Real-time temperature changes were monitored within 5 minutes for each irradiation session (Figures 4E–H and S7). These results indicated an initial rise followed by a gradual decline in the maximum temperature of the tumor, possibly attributed to the progressive elimination of the drug post-administration cessation. Moreover, GNR@TM exhibited a comparatively slower reduction in peak tumor temperature, which could be linked to its high accumulation within the tumor and thus holds promise for future anticancer therapies.

Magnification of the Tumor EPR Effect Induced by NIR Laser

The EPR effect is characterized by the presence of wider gaps in blood vessels within tumors and inflamed tissues, as compared to normal tissues, due to excessive angiogenesis.^{46,47} This allows for extravasation of long-circulating drug-loaded nanoparticles with hydrodynamic diameters exceeding the real clearance threshold from leaky tumor vessels.^{48,49} Once extravasated, nanoparticles are sequestered within the tumor microenvironment, leading to elevated drug concentrations. Following laser irradiation, the local temperature of the GNR@TM/L-treated tumor surface rose to 45 °C (Figure 4G and H). As depicted in Figure 5A–D, intercellular gaps among endothelial cells of tumor blood vessels were expanded, and drug accumulation at tumors was enhanced. Thus, we have demonstrated that laser treatment can magnify the EPR effect of tumors, which may be due to the enhanced permeability of cell membranes and tumor vasculature caused by the temperature rise, leading to elevated concentration of drugs within the tumor.

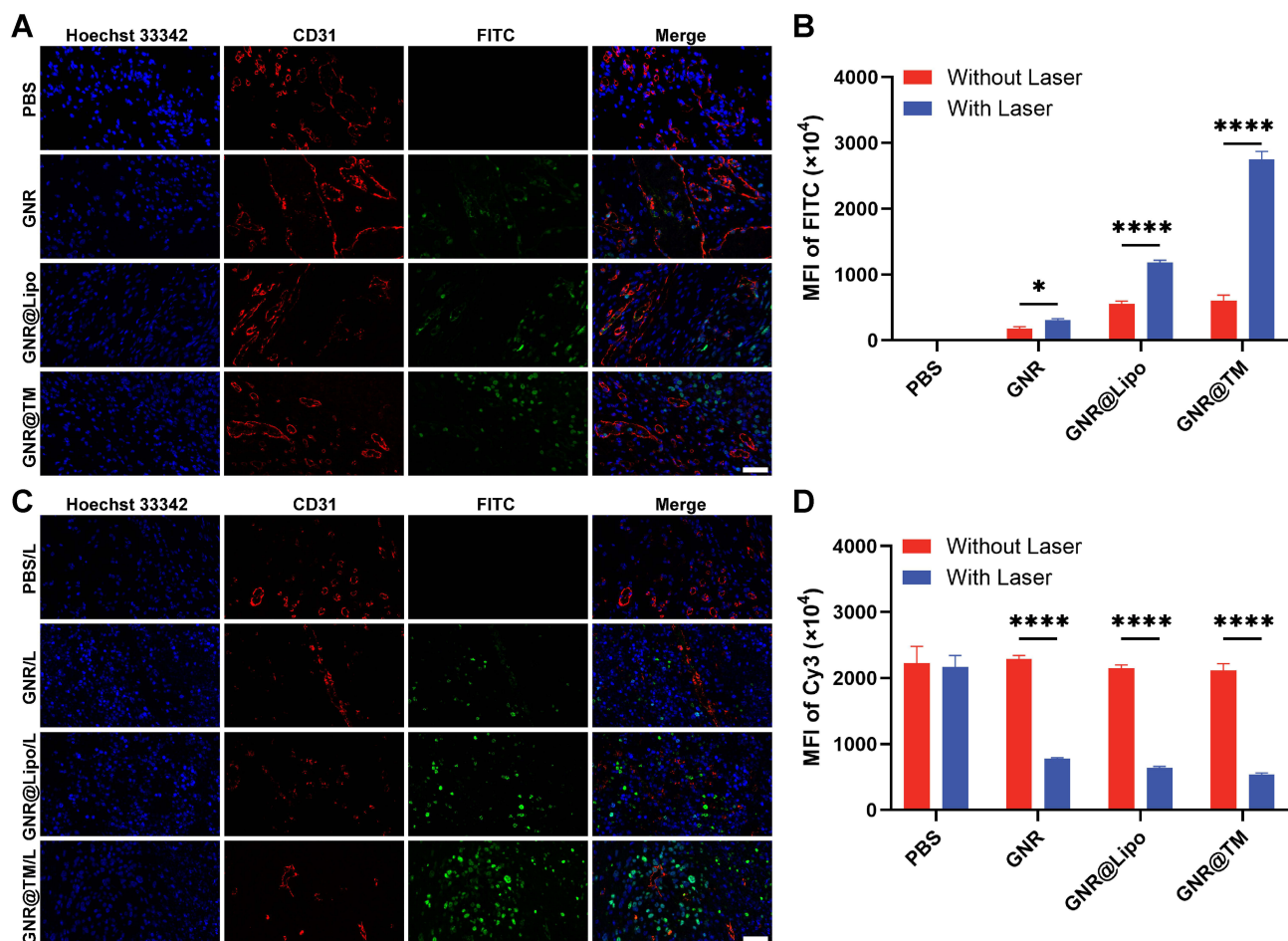


Figure 5 Histological analysis of organs excised from mice that received PBS, GNR, GNR@Lipo and GNR@TM with or without laser irradiation. (A–D) Immunofluorescence staining of Cy3 (CD31) and FITC (GNR) in tumor tissues and corresponding MFI of Cy3 and FITC. Scale bar: 50 μ m. * $P < 0.05$, and **** $P < 0.0001$.

Antitumor Efficacy and Biocompatibility of GNR@TM

To investigate the inhibitory effect on tumor progression, MB49 tumor-bearing mouse models were established to assess the antitumor efficacy of GNR@TM. Tumor volumes and body weights were monitored every two days during treatment (Figures 6A–E and S8). Without near-infrared laser, the GNR@TM group showed minimal inhibition of tumor growth. Due to its superior tumor targeting ability and highly effective photothermal killing performance, the GNR@TM/L group exhibited the slowest tumor growth rate with a final volume of approximately 41 mm³ on day 18, demonstrating the remarkable potential for inhibiting tumor growth. The tumor volume inhibition rate and tumor mass inhibition rate of GNR@TM-mediated PTT treatment reached 96.4% and 97.3% (Figures 6F, S9 and Tables S1, S2). By contrast, tumor growth was initially suppressed in both the GNR/L and GNR@Lipo/L groups, while significant tumor regrowth was observed 6 days after treatment. The mortality rate of mice with tumors was evaluated within a 60-day period. As illustrated in Figure 6G, the number of mice in the PBS, PBS/L, and GNR groups declined rapidly prior to day 45. In contrast, the GNR@TM group exhibited the highest survival rate, accompanied by minimal weight fluctuations (Figure 6H and I), which can be attributed to the satisfactory tumor suppression achieved through GNR@TM-mediated PTT combined with laser irradiation. Furthermore, TUNEL (FITC-dUTP) and H&E staining of tumors confirmed the excellent antitumor efficacy of GNR@TM-mediated PTT (Figures 6J, K and S10), revealing significant pathological changes in tumor.

After confirming tumor suppression, it is also essential to consider biocompatibility and biosafety. Throughout the treatment period, all mice exhibited no abnormal clinical signs or behaviors and gradually gained weight, indicating excellent physical condition (Figure 6H and I). After treatment, key organs were harvested for H&E staining. The resulting images revealed the absence of inflammatory lesions or obvious tissue damage (Figure 6L and M), indicating good biocompatibility and promising potential in biomedical applications of GNR@TM.

Discussion

The EPR effect facilitates the entry of nanomedicines into penetrate the tumor microenvironment and become trapped in the tumors.^{50,51} However, relying solely on the EPR effect appears to be suboptimal in terms of therapeutic efficacy,⁵² and may not be present in all types of tumors. Furthermore, the clinical research outcomes of strategies aimed at enhancing tumor permeability and improving the effectiveness of anti-cancer drug transportation using certain agents have also been disappointing.⁵³ Presently, cancer-directed therapy is mainly accomplished through specific molecular interactions between receptors and ligands targeting surface antigens overexpressed on cancer cells.⁵⁴ Nevertheless, complex factors such as tumor heterogeneity, physiological disorders, and abnormal tumor microenvironment have hindered the translation of nanocapsules from the laboratory to the clinic.⁵⁵ Recent reports have shown that tumor cell membrane-coated nanomaterials with immune escape and homotypic binding capabilities are designed for precise and efficient antitumor therapy.⁵⁶

In this study, we advanced the therapeutic strategy and demonstrated a biomimetic nanoplatform GNR@TM, which was composed of gold nanorods wrapped by the cancer cell membrane. As our results showed, upon irradiation with a 780 nm laser (1.5 W/cm², 5 min), the temperature of GNR@TM rapidly increased to about 55 °C, demonstrating excellent photothermal conversion efficiency and stability (Figure 1). Flow cytometry, CLSM, and TEM all indicated that the cancer cell membrane facilitated the effective uptake of GNR@TM by cells and exhibited low cytotoxicity (Figure 2). Due to the PTT effect, significant cytotoxicity was observed under laser irradiation, which was validated by CCK8 assay, live/dead cell staining, and flow cytometry analysis (Figure 3). Hemolysis assay, minimal differences in mouse tumor weight changes, and H&E staining indicated that GNR@TM exhibited good biocompatibility (Figures 4 and 6). After intravenous injection, the GNR@TM/L group showed high accumulation in tumors (Figure 4D), which can be ascribed to the homologous targeting ability of cancer cell membranes coated on nanorods, long retention in the blood (Figure 4C) and photo-controlled therapy (Figure 5). After laser irradiation, GNR@TM exhibited a significantly stronger temperature increase within 5 minutes (Figure 4H), indicating its good in vivo photothermal performance. Furthermore, upon cessation of administration, the GNR@TM group exhibited the slowest rate of decline in maximum tumor temperature (Figure 4F), which may be attributed to the high aggregation of GNR@TM in tumor sites, laying the

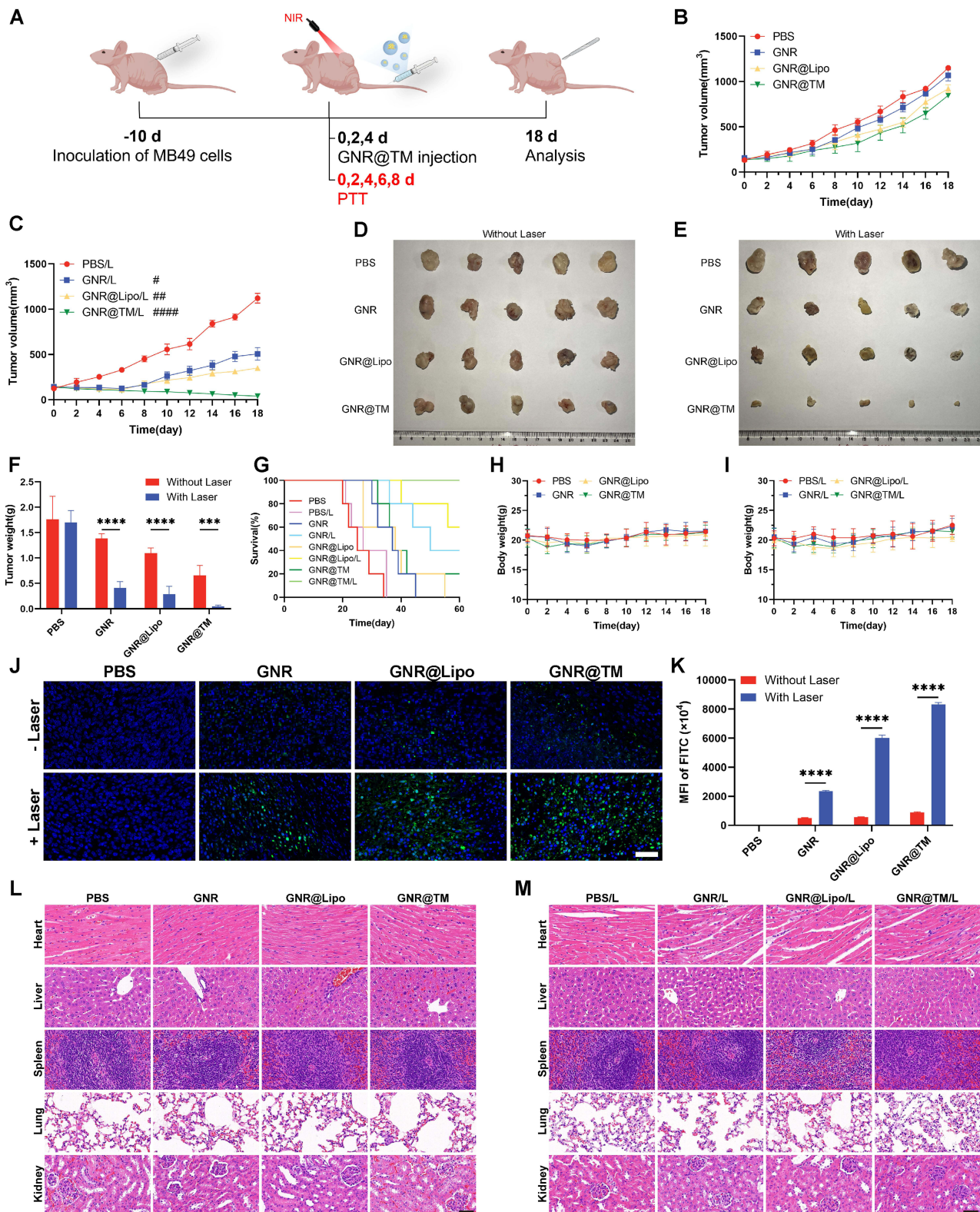


Figure 6 In vivo antitumor effect of GNR@TM. (A) Schematic diagram of administration route for GNR@TM in tumor suppression experiment. (B and C) Tumor volumes of each group with different treatments (n = 5). (D and E) Photographs of the excised tumors in different groups (n = 5). (F) Tumor weights of MB49-bearing mice after various treatments (n = 5). (G) Survival curves of each mouse in different groups (n = 5). (H and I) The body weight of different groups for 18 days (n = 5). (J) Immunofluorescence staining of TUNEL in tumor sites after multiple treatment and corresponding MFI of FITC (K). Scale bar: 50 μ m. (L and M) H&E staining of major organs (heart, liver, spleen, lung, and kidney) after different treatments. Scale bar: 50 μ m. #P < 0.05, ###P < 0.01, and #####P < 0.0001 (# vs PBS group). ***P < 0.001, and ****P < 0.0001.

foundation for subsequent anti-tumor therapy. Due to outstanding tumor targeting ability and efficient photothermal ablation performance, the GNR@TM/L group exhibited a significantly slower tumor growth rate (Figure 6) and demonstrated excellent tumor suppression efficacy. Therefore, the biomimetic nanoplatfrom GNR@TM constructed in this study exhibited high cellular uptake, prolonged blood circulation time, strong tumor penetration, excellent photothermal performance, and superior tumor inhibition. The strategy of cell membrane-camouflaged nanoparticles provides a powerful tool to improve in vivo transport and cellular targeting of nanoparticles for therapeutic purposes.

Cell membrane-camouflaged nanoparticle represents a cell-material composite nanoplatfrom combining the benefits of both organic and artificial components.⁵⁷ Tumor cells play a crucial role in cancer treatment across various cell origins due to their homotypic targeting to tumors and their inherent ability to evade the immune system.^{19,58} The development and progression of cancer involve a series of intricate steps, wherein cancer cell adhesion molecules (CCAMs) play a key part in promoting recurrence, invasion, and distant metastasis.⁵⁹ These CCAMs are involved, either fully or partially, in the adhesive interactions between cancer cells and other types of cells (heterotypic interactions), as well as between cancer cells themselves (homotypic interactions), that lead to the formation and colonization of metastatic tumors. Collectively, functionalization of cancer cell membranes (CCMs) on synthetic nanomaterials allows for immune evasion and exhibits homologous binding ability, leading to a substantial increase in their capacity to accumulate and retain specifically in cancerous tissues.⁶⁰

Due to the EPR effect, gold nanoparticles preferentially accumulate within tumors following intravenous injection.⁶¹ We investigated the impact of near-infrared laser on tumor EPR effect. After irradiation with a 780 nm laser, the temperature of the GNR@TM/L group tumor increased to 45 °C. We found that the intercellular gaps of tumor vascular endothelial cells were enlarged, and the aggregation of GNR@TM in the tumor sites was intensified. Therefore, the laser can induce the magnification of tumor EPR effect. The moderate temperature increase (43–45 °C) is beneficial, not only inducing PTT at high temperatures but also enhancing the permeability of tumors to facilitate the uptake of nanoparticles by tumors without causing cellular damage.⁶² In addition, mild hyperthermia can enhance tumor blood perfusion and augment the permeability of tumor microvessels to facilitate drug accumulation, thereby improving the efficacy of PTT.⁶³ Functional and structural investigations have revealed the existence of sizable pores within tumor vasculature, which facilitate the extravasation of nanoparticles.⁶⁴ As a response to thermal stress, endothelial cells undergo contraction, followed by the widening of intercellular gaps, thereby facilitating the extravasation of larger particles.⁶⁵ The contraction of endothelial cell structure may be attributed to the disintegration of the cellular cytoskeleton following hyperthermia.⁶⁶ Changes in tumor blood flow may serve as a possible mechanism for the accumulation of drugs induced by hyperthermia. An elevation in overall blood flow can facilitate more nanoparticles to perfuse through tumor vasculature, ultimately leading to increased extravasation.

Conclusion

In conclusion, we have created a NIR-triggered nanomedicine GNR@TM. Specifically, after constructing GNRs, the cell membrane TM was coated onto them. With the assistance of homotypic tumor cell membranes, GNR@TM nanocomplexes carrying photosensitizers preferentially accumulated at the tumor site, and then TM could be discarded to ensure exposure of GNRs for PTT to generate tumor toxicity. In addition, the slight temperature elevation at the tumor site induced by the photothermal effect further enhanced the accumulation of GNR@TM within tumors, enhancing its PTT efficacy. In conclusion, our approach provided a promising biomimetic nanoplatfrom that increased intratumor drug accumulation via photo-controlled therapy and bio-membrane regulated active targeting for highly targeted tumor ablation.

Acknowledgments

This work was financially supported by the National Natural Science Foundation of China (92059112, 82072821 and 31470964), the Program of Shanghai Academic/Technology Research Leader (22XD1404700), University of Shanghai for Science and Technology (10-21-302-405), and the Shanghai Songjiang Municipal Science and Technology Commission Natural Science Foundation (20SJKJGG250).

Disclosure

The authors report no conflicts of interest in this work.

References

- Ogihara T, Mizoi K, Kamioka H, Yano K. Physiological roles of ERM proteins and transcriptional regulators in supporting membrane expression of efflux transporters as factors of drug resistance in cancer. *Cancers*. 2020;12(11):3352. doi:10.3390/cancers12113352
- Solaki M, Ewald JC. Fueling the cycle: CDKs in carbon and energy metabolism. *Front Cell Dev Biol*. 2018;6. doi:10.3389/fcell.2018.00093
- Blanco E, Shen H, Ferrari M. Principles of nanoparticle design for overcoming biological barriers to drug delivery. *Nat Biotechnol*. 2015;33(9):941–951. doi:10.1038/nbt.3330
- Shi J, Kantoff PW, Wooster R, Farokhzad OC. Cancer nanomedicine: progress, challenges and opportunities. *Nat Rev Cancer*. 2017;17(1):20–37. doi:10.1038/nrc.2016.108
- Sun Q, Zhou Z, Qiu N, Shen Y. Rational design of cancer nanomedicine: nanoproperty integration and synchronization. *Adv Mater* 2017;29(14):1606628. doi:10.1002/adma.201606628
- Prabhakar U, Maeda H, Jain RK, et al. Challenges and key considerations of the enhanced permeability and retention effect for nanomedicine drug delivery in oncology. *Cancer Res*. 2013;73(8):2412–2417. doi:10.1158/0008-5472.CAN-12-4561
- Ruenaroengsak P, Cook JM, Florence AT. Nanosystem drug targeting: facing up to complex realities. *J Control Release*. 2010;141(3):265–276. doi:10.1016/j.jconrel.2009.10.032
- Sindhvani S, Syed AM, Ngai J, et al. The entry of nanoparticles into solid tumours. *Nat Mater*. 2020;19(5):566–575. doi:10.1038/s41563-019-0566-2
- Zhu M, Zhuang J, Li Z, et al. Machine-learning-assisted single-vessel analysis of nanoparticle permeability in tumour vasculatures. *Nat Nanotechnol*. 2023;18(6):657–666. doi:10.1038/s41565-023-01323-4
- Mu Q, Jiang G, Chen L, et al. Chemical basis of interactions between engineered nanoparticles and biological systems. *Chem Rev*. 2014;114(15):7740–7781. doi:10.1021/cr400295a
- Wu L, Lin B, Yang H, et al. Enzyme-responsive multifunctional peptide coating of gold nanorods improves tumor targeting and photothermal therapy efficacy. *Acta Biomater*. 2019;86:363–372. doi:10.1016/j.actbio.2019.01.026
- Yang B, Chen Y, Shi J. Reactive oxygen species (ROS)-based nanomedicine. *Chem Rev*. 2019;119(8):4881–4985. doi:10.1021/acs.chemrev.8b00626
- Li W, Zhao H, Qian W, et al. Chemotherapy for gastric cancer by finely tailoring anti-Her2 anchored dual targeting immunomicelles. *Biomaterials*. 2012;33(21):5349–5362. doi:10.1016/j.biomaterials.2012.04.016
- Cho HJ, Yoon HY, Koo H, et al. Self-assembled nanoparticles based on hyaluronic acid-ceramide (HA-CE) and Pluronic® for tumor-targeted delivery of docetaxel. *Biomaterials*. 2011;32(29):7181–7190. doi:10.1016/j.biomaterials.2011.06.028
- Zhen X, Cheng P, Pu K. Recent advances in cell membrane-camouflaged nanoparticles for cancer phototherapy. *Small*. 2019;15(1):1804105. doi:10.1002/smll.201804105
- Xuan M, Shao J, Li J. Cell membrane-covered nanoparticles as biomaterials. *Natl Sci Rev*. 2019;6(3):551–561. doi:10.1093/nsr/nwz037
- Du Y, Qian X, Lin F, et al. A biomimetic nanoplatform for precise reprogramming of tumor-associated macrophages and NIR-II mediated antitumor immune activation. *Acta Biomater*. 2023;162:85–97. doi:10.1016/j.actbio.2023.03.021
- Yang H, Ding Y, Tong Z, et al. pH-responsive hybrid platelet membrane-coated nanobomb with deep tumor penetration ability and enhanced cancer thermal/chemodynamic therapy. *Theranostics*. 2022;12(9):4250–4268. doi:10.7150/thno.68996
- Fang RH, Hu CMJ, Luk BT, et al. Cancer cell membrane-coated nanoparticles for anticancer vaccination and drug delivery. *Nano Lett*. 2014;14(4):2181–2188. doi:10.1021/nl500618u
- Wang J, Sun J, Hu W, et al. A porous Au@Rh bimetallic core-shell nanostructure as an H₂ O₂-driven oxygenerator to alleviate tumor hypoxia for simultaneous bimodal imaging and enhanced photodynamic therapy. *Adv Mater* 2020;32(22):2001862. doi:10.1002/adma.202001862
- Lv P, Liu X, Chen X, et al. Genetically engineered cell membrane nanovesicles for oncolytic adenovirus delivery: a versatile platform for cancer virotherapy. *Nano Lett*. 2019;19(5):2993–3001. doi:10.1021/acs.nanolett.9b00145
- Zhang P, Liu G, Chen X. Nanobiotechnology: cell membrane-based delivery systems. *Nano Today*. 2017;13:7–9. doi:10.1016/j.nantod.2016.10.008
- Qi P, Zhang J, Bao Z, Liao Y, Liu Z, Wang J. A platelet-mimicking single-atom nanozyme for mitochondrial damage-mediated mild-temperature photothermal therapy. *ACS Appl Mater Interfaces*. 2022;14(17):19081–19090. doi:10.1021/acsami.1c22346
- Vankayala R, Hwang KC. Near-infrared-light-activatable nanomaterial-mediated phototheranostic nanomedicines: an emerging paradigm for cancer treatment. *Adv Mater* 2018;30(23):1706320. doi:10.1002/adma.201706320
- Dreaden EC, Alkilany AM, Huang X, Murphy CJ, El-Sayed MA. The golden age: gold nanoparticles for biomedicine. *Chem Soc Rev*. 2012;41(7):2740–2779. doi:10.1039/C1CS15237H
- Kesharwani P, Ma R, Sang L, et al. Gold nanoparticles and gold nanorods in the landscape of cancer therapy. *Mol Cancer*. 2023;22(1):98. doi:10.1186/s12943-023-01798-8
- Huang L, Zhou M, Abbas G, et al. A cancer cell membrane-derived biomimetic nanocarrier for synergistic photothermal/gene therapy by efficient delivery of CRISPR/Cas9 and gold nanorods. *Adv Healthc Mater*. 2022;11(16). doi:10.1002/adhm.202201038
- Yang H, Tong Z, Sun S, Mao Z. Enhancement of tumour penetration by nanomedicines through strategies based on transport processes and barriers. *J Control Release*. 2020;328:28–44. doi:10.1016/j.jconrel.2020.08.024
- Maeda H, Nakamura H, Fang J. The EPR effect for macromolecular drug delivery to solid tumors: improvement of tumor uptake, lowering of systemic toxicity, and distinct tumor imaging in vivo. *Adv Drug Deliv Rev*. 2013;65(1):71–79. doi:10.1016/j.addr.2012.10.002
- Li S, Zhang Y, Wang J, et al. Nanoparticle-mediated local depletion of tumour-associated platelets disrupts vascular barriers and augments drug accumulation in tumours. *Nat Biomed Eng*. 2017;1(8):667–679. doi:10.1038/s41551-017-0115-8
- Tao W, Zhao D, Li G, et al. Artificial tumor microenvironment regulated by first hemorrhage for enhanced tumor targeting and then occlusion for synergistic bioactivation of hypoxia-sensitive plasmids. *Acta Pharm Sin B*. 2022;12(3):1487–1499. doi:10.1016/j.apsb.2021.08.010
- Setyawati MI, Wang Q, Ni N, et al. Engineering tumoral vascular leakiness with gold nanoparticles. *Nat Commun*. 2023;14(1):4269. doi:10.1038/s41467-023-40015-4

33. Satterlee AB, Rojas JD, Dayton PA, Huang L. Enhancing nanoparticle accumulation and retention in desmoplastic tumors via vascular disruption for internal radiation therapy. *Theranostics*. 2017;7(2):253–269. doi:10.7150/thno.16681
34. Volz J, Mammadova-Bach E, Gil-Pulido J, et al. Inhibition of platelet GPVI induces intratumor hemorrhage and increases efficacy of chemotherapy in mice. *Blood*. 2019;133(25):2696–2706. doi:10.1182/blood.2018877043
35. Cabral H, Matsumoto Y, Mizuno K, et al. Accumulation of sub-100 nm polymeric micelles in poorly permeable tumours depends on size. *Nat Nanotechnol*. 2011;6(12):815–823. doi:10.1038/nnano.2011.166
36. Oei AL, Kok HP, Oei SB, et al. Molecular and biological rationale of hyperthermia as radio- and chemosensitizer. *Adv Drug Deliv Rev*. 2020;163–164:84–97. doi:10.1016/j.addr.2020.01.003
37. Alkilany AM, Thompson LB, Boulos SP, Sisco PN, Murphy CJ. Gold nanorods: their potential for photothermal therapeutics and drug delivery, tempered by the complexity of their biological interactions. *Adv Drug Deliv Rev*. 2012;64(2):190–199. doi:10.1016/j.addr.2011.03.005
38. Chen Q, Huang G, Wu W, et al. A hybrid eukaryotic-prokaryotic nanoplatform with photothermal modality for enhanced antitumor vaccination. *Adv Mater*. 2020;32(16):e1908185. doi:10.1002/adma.201908185
39. Liu WL, Zou MZ, Liu T, et al. Cytomembrane nanovaccines show therapeutic effects by mimicking tumor cells and antigen presenting cells. *Nat Commun*. 2019;10(1):3199. doi:10.1038/s41467-019-11157-1
40. Wang L, Liu Y, Li W, et al. Selective targeting of gold nanorods at the mitochondria of cancer cells: implications for cancer therapy. *Nano Lett*. 2011;11(2):772–780. doi:10.1021/nl103992v
41. Zhang F, Hou Y, Zhu M, et al. Death pathways of cancer cells modulated by surface molecule density on gold nanorods. *Adv. Sci.* 2021;8(22):2102666. doi:10.1002/advs.202102666
42. Overgaard J. Effect of hyperthermia on malignant cells in vivo. A review and a hypothesis. *Cancer*. 1977;39(6):2637–2646. doi:10.1002/1097-0142(197706)39:6<2637::aid-cnrc2820390650>3.0.co;2-s
43. An J, Hu YG, Li C, et al. A pH/ultrasound dual-response biomimetic nanoplatform for nitric oxide gas-sonodynamic combined therapy and repeated ultrasound for relieving hypoxia. *Biomaterials*. 2020;230:119636. doi:10.1016/j.biomaterials.2019.119636
44. Puleio R, Licciardi M, Varvara P, et al. Effect of actively targeted copolymer coating on solid tumors eradication by gold nanorods-induced hyperthermia. *Int J Pharm*. 2020;587:119641. doi:10.1016/j.ijpharm.2020.119641
45. Arunkumar P, Raju B, Vasantharaja R, et al. Near infra-red laser mediated photothermal and antitumor efficacy of doxorubicin conjugated gold nanorods with reduced cardiotoxicity in Swiss albino mice. *Nanomedicine*. 2015;11(6):1435–1444. doi:10.1016/j.nano.2015.03.012
46. Arroyo AG, Iruela-Arispe ML. Extracellular matrix, inflammation, and the angiogenic response. *Cardiovasc Res*. 2010;86(2):226–235. doi:10.1093/cvr/cvq049
47. Haley B, Frenkel E. Nanoparticles for drug delivery in cancer treatment. *Urol Oncol*. 2008;26(1):57–64. doi:10.1016/j.urolonc.2007.03.015
48. Sharifi M, Cho WC, Ansariesfahani A, et al. An updated review on EPR-based solid tumor targeting nanocarriers for cancer treatment. *Cancers*. 2022;14(12):2868. doi:10.3390/cancers14122868
49. Liu T, Wang C, Cui W, et al. Combined photothermal and photodynamic therapy delivered by PEGylated MoS₂ nanosheets. *Nanoscale*. 2014;6(19):11219–11225. doi:10.1039/c4nr03753g
50. Zhao X, Li F, Li Y, et al. Co-delivery of HIF1 α siRNA and gemcitabine via biocompatible lipid-polymer hybrid nanoparticles for effective treatment of pancreatic cancer. *Biomaterials*. 2015;46:13–25. doi:10.1016/j.biomaterials.2014.12.028
51. Grodzinski P, Farrell D. Future opportunities in cancer nanotechnology—NCI strategic workshop report. *Cancer Res*. 2014;74(5):1307–1310. doi:10.1158/0008-5472.CAN-13-2787
52. Wilhelm S, Tavares AJ, Dai Q, et al. Analysis of nanoparticle delivery to tumours. *Nat Rev Mater*. 2016;1(5):16014. doi:10.1038/natrevmats.2016.14
53. Maeda H. Nitroglycerin enhances vascular blood flow and drug delivery in hypoxic tumor tissues: analogy between angina pectoris and solid tumors and enhancement of the EPR effect. *J Control Release*. 2010;142(3):296–298. doi:10.1016/j.jconrel.2010.01.002
54. Ruoslahti E, Bhatia SN, Sailor MJ. Targeting of drugs and nanoparticles to tumors. *J Cell Biol*. 2010;188(6):759–768. doi:10.1083/jcb.200910104
55. Chauhan VP, Jain RK. Strategies for advancing cancer nanomedicine. *Nat Mater*. 2013;12(11):958–962. doi:10.1038/nmat3792
56. Wang R, Yang H, Fu R, et al. Biomimetic upconversion nanoparticles and gold nanoparticles for novel simultaneous dual-modal imaging-guided photothermal therapy of cancer. *Cancers*. 2020;12(11):3136. doi:10.3390/cancers12113136
57. Kroll AV, Fang RH, Zhang L. Biointerfacing and applications of cell membrane-coated nanoparticles. *Bioconjug Chem*. 2017;28(1):23–32. doi:10.1021/acs.bioconjchem.6b00569
58. Sun H, Su J, Meng Q, et al. Cancer cell membrane-coated gold nanocages with hyperthermia-triggered drug release and homotypic target inhibit growth and metastasis of breast cancer. *Adv Funct Mater*. 2017;27(3):1604300. doi:10.1002/adfm.201604300
59. Okegawa T, Pong RC, Li Y, Hsieh JT. The role of cell adhesion molecule in cancer progression and its application in cancer therapy. *Acta Biochim Pol*. 2004;51(2):445–457. doi:10.18388/abp.2004_3583
60. Sun H, Su J, Meng Q, et al. Cancer-cell-biomimetic nanoparticles for targeted therapy of homotypic tumors. *Adv Mater* 2016;28(43):9581–9588. doi:10.1002/adma.201602173
61. Liu Y, Ashton JR, Moding EJ, et al. A plasmonic gold nanostar theranostic probe for in vivo tumor imaging and photothermal therapy. *Theranostics*. 2015;5(9):946–960. doi:10.7150/thno.11974
62. Yi X, Yang K, Liang C, et al. Imaging-guided combined photothermal and radiotherapy to treat subcutaneous and metastatic tumors using iodine-131-doped copper sulfide nanoparticles. *Adv Funct Mater*. 2015;25(29):4689–4699. doi:10.1002/adfm.201502003
63. Chu KF, Dupuy DE. Thermal ablation of tumours: biological mechanisms and advances in therapy. *Nat Rev Cancer*. 2014;14(3):199–208. doi:10.1038/nrc3672
64. Yuan F. Transvascular drug delivery in solid tumors. *Semin Radiat Oncol*. 1998;8(3):164–175. doi:10.1016/s1053-4296(98)80042-8
65. Gaber MH, Wu NZ, Hong K, Huang SK, Dewhirst MW, Papahadjopoulos D. Thermosensitive liposomes: extravasation and release of contents in tumor microvascular networks. *Int J Radiat Oncol Biol Phys*. 1996;36(5):1177–1187. doi:10.1016/s0360-3016(96)00389-6
66. Dermietzel R, Streffer C. The cytoskeleton and proliferation of melanoma cells under hyperthermal conditions. A correlative double immunolabeling study. *Strahlenther Onkol*. 1992;168(10):593–602.

International Journal of Nanomedicine

Dovepress

Publish your work in this journal

The International Journal of Nanomedicine is an international, peer-reviewed journal focusing on the application of nanotechnology in diagnostics, therapeutics, and drug delivery systems throughout the biomedical field. This journal is indexed on PubMed Central, MedLine, CAS, SciSearch[®], Current Contents[®]/Clinical Medicine, Journal Citation Reports/Science Edition, EMBase, Scopus and the Elsevier Bibliographic databases. The manuscript management system is completely online and includes a very quick and fair peer-review system, which is all easy to use. Visit <http://www.dovepress.com/testimonials.php> to read real quotes from published authors.

Submit your manuscript here: <https://www.dovepress.com/international-journal-of-nanomedicine-journal>